Remote Sensing of Environment 123 (2012) 127–138

Contents lists available at SciVerse ScienceDirect

Remote Sensing of Environment

journal homepage: www.elsevier.com/locate/rse

A decadal investigation of supraglacial lakes in West Greenland using a fully automatic detection and tracking algorithm

Yu-Li Liang [a,*,1], William Colgan [b,1], Qin Lv [a], Konrad Steffen [b,c], Waleed Abdalati [b,c,d], Julienne Stroeve [b,e], David Gallaher [b,e], Nicolas Bayou [b,c]

[a] Department of Computer Science, University of Colorado, Boulder, CO, 80309-0430, United States
[b] Cooperative Institute for Research in Environmental Sciences, University of Colorado, Boulder, CO, 80309-0216, United States
[c] Department of Geography, University of Colorado, Boulder, CO, 80309-0260, United States
[d] Headquarters, National Aeronautic and Space Administration, Washington, DC, 20546, United States
[e] National Snow and Ice Data Center, University of Colorado, Boulder, CO, 80309-0449, United States

ARTICLE INFO

Article history:
Received 28 October 2011
Received in revised form 15 March 2012
Accepted 17 March 2012
Available online 13 April 2012

Keywords:
Change detection
Temporal tracking
MODIS
Greenland Ice Sheet
Supraglacial lake
Melt intensity

ABSTRACT

The sudden drainage of supraglacial lakes has been previously observed to initiate surface-to-bed hydrologic connections, which are capable of enhancing basal sliding, in regions of the Greenland Ice Sheet where ice thickness approaches 1 km. In this study, we develop a robust algorithm, which automatically detects and tracks individual supraglacial lakes using visible satellite imagery, to document the evolution of a population of West Greenland supraglacial lakes over ten consecutive melt seasons. Validation tests indicate that the algorithm is highly accurate: 99.0% of supraglacial lakes can be detected and tracked and 96.3% of reported lakes are true supraglacial lakes with accurate lake properties, such as lake area, and timing of formation and drainage. Investigation of the interannual evolution of supraglacial lakes in the context of annual melt intensity reveals that during more intense melt years, supraglacial lakes drain more frequently and earlier in the melt season. Additionally, the lake population extends to higher elevations during more intense melt years, exposing an increased inland area of the ice sheet to sudden lake drainage events. These observations suggest that increased surface meltwater production due to climate change will enhance the spatial extent and temporal frequency of lake drainage events. It is unclear whether this will ultimately increase or decrease the basal sliding sensitivity of interior regions of the Greenland Ice Sheet.

1. Introduction

An acceleration of sea level rise due to mass loss from the Greenland Ice Sheet has been recently observed. While Greenland contributed 0.21 mm/year of sea level rise between 1993 and 2003, its contribution increased to ~0.5 mm/year between 2003 and 2007. During this latter period, the observed total sea level rise (from all sources) was ~2.4 mm/year (Cazenave & Llovel, 2010). Current mass loss from the Greenland Ice Sheet appears to be equally split between runoff from surface ablation and iceberg calving (Shepherd & Wingham, 2007; Van den Broeke et al., 2009). It has been speculated that relatively small increases in surface meltwater production, due to a warming climate, may result in disproportionately large increases in ice discharge via basal sliding (Bartholomew et al., 2010; Zwally et al., 2002). While observational evidence clearly indicates a link between increased surface meltwater production and enhanced basal sliding velocity on a variety of time-scales (Bartholomew et al., 2010; Joughin et al., 2008; Shepherd et al., 2009; Zwally et al., 2002), several studies suggest that an increase in surface meltwater production could result in an earlier seasonal transition to a more efficient subglacial drainage system, and hence a net decrease in mean annual basal sliding velocity (Schoof, 2010; Sundal et al., 2011; Van de Wal et al., 2008).

As large volumes of water are required to propagate crevasses to the bed via hydrofracture (Van der Veen, 2007), supraglacial lakes can play an important role in establishing hydrologic connections between the supra- and sub-glacial hydrologic systems. These near vertical hydrologic connections, known as “moulins”, can rapidly route surface water to the bed, where it pressurizes the subglacial environment and reduces basal friction (Das et al., 2008; Zwally et al., 2002). Temporal and spatial variability in meltwater delivery to the subglacial hydrologic system enhances basal sliding velocities (Schoof, 2010). Moulins, which collect surface meltwater from a relatively large area of the ice sheet, are more efficient in enhancing basal

* Corresponding author. Tel.: +1 303 492 7514.
E-mail addresses: Yu-Li.Liang@colorado.edu (Y.-L. Liang), William.Colgan@colorado.edu (W. Colgan), Qin.Lv@colorado.edu (Q. Lv), Konrad.Steffen@colorado.edu (K. Steffen), Waleed.Abdalati@colorado.edu (W. Abdalati), Stroeve@nsidc.org (J. Stroeve), David.Gallaher@nsidc.org (D. Gallaher), Nicolas.Bayou@colorado.edu (N. Bayou).
[1] Equally contributed.

0034-4257 © 2012 Elsevier Inc. Open access under CC BY-NC-ND license.
doi:10.1016/j.rse.2012.03.020

sliding than crevasse-type drainage networks, which relatively attenuate the surface meltwater pulse at diurnal and other time-scales (Colgan et al., 2011). Studies have documented that the sudden drainage of supraglacial lakes results in substantial increases in basal sliding velocity (Das et al., 2008; Joughin et al., 1996, 2008; Shepherd et al., 2009). While the velocity anomalies stemming from lake drainage events are typically local in extent and short in duration, the cumulative effect of multiple lake drainages could potentially produce a significant regional summer ice acceleration (Das et al., 2008; Hoffman et al., 2011). The sudden drainage of supraglacial lakes appears to be a key factor in creating moulins in areas of thick ice (i.e., >1 km) that would not otherwise experience rapid surface-to-bed hydrologic connectively (Krawczynski et al., 2009; Pimentel & Flowers, 2011; Shepherd et al., 2009; Sundal et al., 2009). Thus, a potential increase in the extent and/or frequency of lake drainage events is expected to increase the extent and/or frequency of surface-to-bed hydrologic connections in the interior regions of the ice sheet (where ice thickness exceeds 1 km). This provides an impetus to understand how the spatial and temporal distributions of supraglacial lakes, and their associated drainage events, can be expected to respond to increased surface meltwater production in a warming climate.

Several studies have investigated Greenland supraglacial lakes using visible and near infrared satellite imagery. Many of these studies, however, rely on manual interpretation to track supraglacial lakes through time, which is not feasible for long-term and large-scale studies. For example, (McMillan et al., 2007) studied the evolution of 292 lakes over 12 Advanced Spaceborne Thermal Emission and Reflection Radiometer (ASTER) images using manual identification of the lakes. Similarly, Lampkin and VanderBerg (2011) manually digitized 1180 lakes for 3 days in 2007 using Landsat-7 Enhanced Thematic Mapper plus (ETM+) images. Box and Ski (2007) introduced a method to automatically detect supraglacial lakes in individual images, based on prescribed thresholds between various visible and near infrared bands in Moderate Resolution Imaging Spectroradiometer (MODIS) imagery, and then manually tracked the detected lakes in 170 manually selected cloud-free images over 5 years. Sundal et al. (2009) further improved the contours of classified lakes in each image, yet continued to manually track lakes through sequential images (i.e., 268 manually selected cloud-free MODIS images over 4 years). While several of these studies have automated the process of detecting lakes within a single image, all of them require the user to pre-select cloud-free images and manually track individual lakes between sequential images.

A semi-automated lake tracking approach was recently proposed by Selmes et al., 2011. Making the assumption that lake position remains fixed by bedrock topography (i.e., lakes do not advect with ice flow), lakes were automatically detected in individual visible MODIS images. A temporal subset of images (~30 per melt season) was then selected to superimpose into a single aggregate image to show the maximum extent of all detected lakes over five years. However, before superimposing multiple images to create the aggregate image, false positive lakes (e.g., cloud shadows) had to be manually removed from the subset images.

In this study we investigate a population of supraglacial lakes over ten consecutive melt seasons (2000 to 2009) in a 16,500 km^2 area of the Greenland Ice Sheet centered on Jakobshavn Isbrae, West Greenland, using 9040 daily MODIS images. Since manual or partially-manual schemes are impractical to detect and track such a large population of supraglacial lakes, we develop a robust algorithm (Section 2) to automatically detect and track supraglacial lakes using MODIS visible imagery. This algorithm is capable of selecting high-quality images (i.e., fully or partially cloud-free images), detecting and tracking supraglacial lakes and removing false positives, all without manual intervention. Evaluation of the algorithm shows that the algorithm successfully tracks lakes with high accuracy (Section 3). The interannual evolution of the tracked supraglacial lakes is then evaluated in the context of annual melt intensity (Section 4), followed by a discussion on the implications for the Greenland Ice Sheet (Section 5).

2. Lake tracking algorithm

2.1. Data

This study uses daily MODIS band 1 top-of-the atmosphere (TOA) reflectance data (650 nm; visible) at 250 m spatial resolution (Level 1B MOD02 data, http://modis.gsfc.nasa.gov/, (Hall et al., 2007)), from 2000 to 2009, for an approximately 16,500 km^2 study area extending from 68.06°N to 70.43°N and 48.27°W to 51.92°W in West Greenland (Fig. 1). Similar to Sundal et al. (2009), we take the melt season as May 1st to October 1st, a sufficiently long period of time to encompass the full range of seasonal changes in lake area. Visible MODIS data at 250 m and/or 500 m spatial resolution have been used in previous studies detecting supraglacial lakes on the Greenland Ice Sheet (Box & Ski, 2007; Selmes et al., 2011; Sundal et al., 2009). While MODIS reflectance data at 250 m spatial resolution are available for both band 1 (650 nm; visible) and band 2 (857 nm; near infrared), only band 1 reflectance data were used. This is because even though the reflectance contrast between lakes and snow or dry bare ice surfaces is higher in the near-infrared, the contrast between lakes and wet snow/ices is higher in the visible than the near infrared (Warren, 1982). Thus, the algorithm is able to detect lakes even when the surrounding surface is undergoing melt.

In order to flag cloudy pixels and determine the spatial extent of the ice sheet, the corresponding MOD10-L2 product was used to provide a cloud mask and binary snow extent mask at 500 m spatial resolution (Hall et al., 2006). The MOD10-L2 cloud mask has been shown to be unreliable over snow-covered surfaces (Ault et al., 2006). In Sections 2.2 and 2.3, we describe how errors in the cloud mask are handled by the algorithm. Both the snow cover extent and the cloud mask were resampled to 250 m resolution. Hereafter, we refer to the retrieved distributions of cloud and snow as “cloud mask” and “snow mask” respectively. All data were georectified into the Equal-Area Scalable Earth Grid (EASE-Grid) using the MS2GT tool available from the US National Snow and Ice Data Center (Haran, 2003). In total, 9040 MOD02 images and 9040 MOD10-L2 images, spanning the 2000 to 2009 melt seasons, were downloaded, pre-processed, and analyzed by the algorithm

2.2. Automatic Image Selection

Since the algorithm tracks lakes in cloud-free regions within the ice sheet (i.e., cloud-free ice sheet), the first processing step was to mask out all non-ice sheet areas from the images (i.e., land and ocean). Towards this end, a single ice sheet mask was generated for each year based on all available daily MOD10-L2 snow masks. Because snow masks may include cloudy pixels (e.g., Fig. 2(a)), aggregating multiple snow masks helps to ensure all ice sheet pixels in our study region are included. The composite annual ice sheet mask contains all pixels identified as snow for more than 50% of the melt season (e.g., Fig. 2(d)). Finally, using the annual ice sheet mask and daily cloud mask from MOD10-L2, a “valid region” for each image was produced (e.g., Fig. 2(e)). The valid region denotes the cloud-free ice sheet area used by lake-tracking algorithm.

The next step was to select the “highest quality” daily MOD02 image for input to the lake detection/tracking algorithm. This step screens out poor quality images and decreases uncertainty in the final results. Typically, several MOD02 images cover the study area each day. To select the highest quality image for a particular day, four properties are simultaneously evaluated: (P_1) the percentage of cloud-free ice sheet, (P_2) the mean reflectance of MOD02 pixels

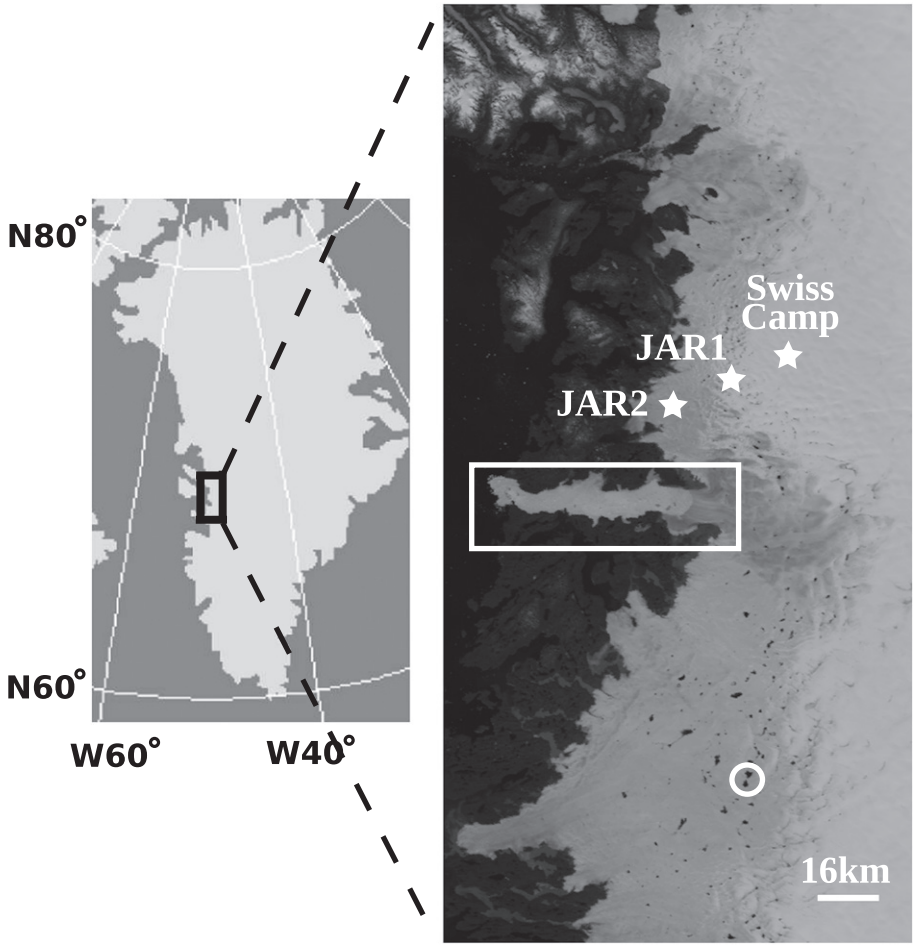

Fig. 1. Left: The black rectangle denotes the study area (68.06°N to 70.43°N and 48.27°W to 51.92°W) in West Greenland. Right: A MODIS MOD02 250 m reflectance image (optical wavelength: 620 nm to 670 nm) acquired on July 8th, 2009. The white rectangle encloses Jakobshavn Fiord. Jakobshavn Isbrae flows from east to west. The white circle denotes a single supraglacial lake. White stars denote the locations of three weather stations (Crawford Point is located 96 km northeast of Swiss Camp and outside the study area).

located in cloud-free ice sheet, (P_3) the sum of the local spatial gradients in the MOD02 reflectance, and (P_4) number of possible lake pixels present in a given MOD02 image.

The first property seeks to maximize the percentage of the cloud-free ice sheet. The second property seeks to maximize the contrast between relatively high reflectance of the snow/ice pixels and relatively low reflectance of the supraglacial lakes pixels. The third property, the sum of local spatial gradients in reflectance, is higher in "sharper" images. This property is defined as the sum of the 1st derivatives of reflectance in both the x and y directions over a distance of 1 pixel. Finally, P_4 ensures that possible lakes are indeed present in the image before the data is input into the lake detection/tracking

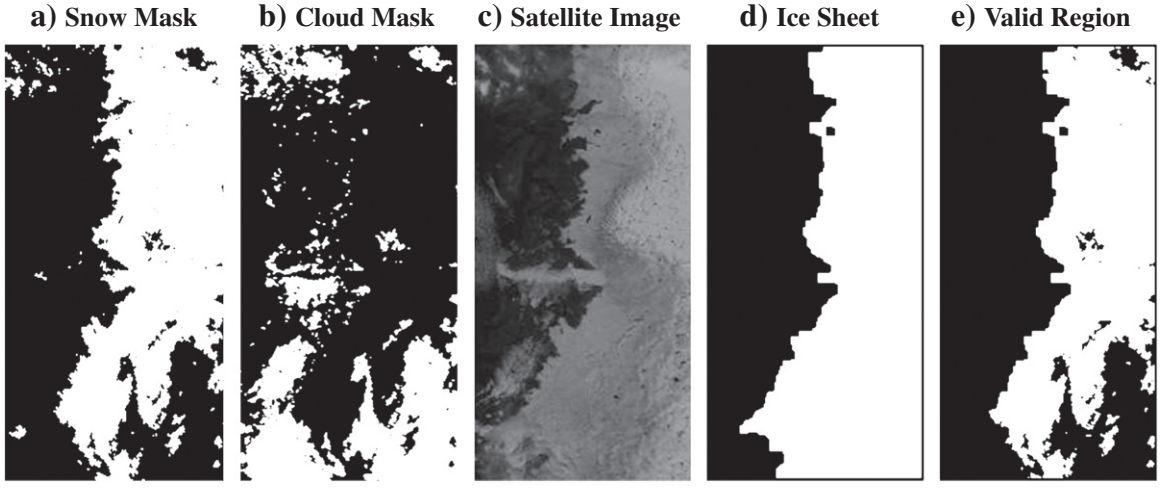

Fig. 2. Developing a daily valid region: (a)–(c) are input images on July 30th, 2006: (a) Snow mask (white pixels: snow). (b) Could mask (white pixels: cloud). (c) MOD02 image. (d) Ice sheet mask for year 2006 (white pixels: ice sheet). (e) Valid region, where the algorithm tracks lakes, for July 30th, 2006 (white pixels: cloud-free ice sheet).

algorithm. The process of detecting possible lakes in each image is described in Section 2.3. No subsequent analysis is performed when $P_4 = 0$. This can occur either when all surface water is frozen, or the entire study area is covered by clouds.

The resulting quality score is defined as the normalized sum of each of the four properties (i.e., the sum of each property divided by its maximum for a given day) and the image with the highest quality score is subsequently selected for analysis (Fig. 3). All selected images also need to meet minimum thresholds. Specifically, images cannot be too cloudy ($P_1 > 30\%$ of annual ice sheet mask), or too dark ($P_2 > 0.15$), and must contain possible lakes pixels ($P_4 > 0$). While any two successive images should ideally be 1 day apart, high quality images are not necessarily available every day after automated image selection. From the initial 9040 MOD02 images, 893 were automatically selected as high quality. Over the ten year study period, the mean duration between two successive images is 1.7 days.

2.3. Automatic supraglacial lake detection and tracking

In the visible portion of the electromagnetic spectrum, lake pixels have a relatively low reflectance in comparison to ice pixels. The algorithm uses this intrinsic property to detect individual lakes by calculating the difference in reflectance between a given pixel and its surrounding neighborhood using a 25×25 pixel moving window. The size of the moving window influences the size of detected lakes. Our choice of a 25×25 pixel window is designed to capture lakes that have one dimension, in either the x or y axis, smaller than 25 pixels (i.e., 6250 m). Box & Ski (2007) studied supraglacial lakes near Jakobshavn Isbrae and found the largest lake area to be ~16.9 km^2. If the maximum lake area is approximated with a square, it is smaller than a 5 km × 5 km window (i.e., 20×20 pixels). Thus, our choice of window size (i.e., 25×25 pixels) is expected to capture all supraglacial lakes in the study region. For each pixel, the neighborhood reflectance is calculated as the weighted mean of reflectance within the moving window. The algorithm puts a greater weight on the reflectance of pixels closer to the center of the window than pixels at the edge of the window. The reflectance difference of each pixel is then determined by subtracting the center pixel reflectance from the neighborhood reflectance.

The algorithm computes one threshold to classify the lakes in each image of each day. For each image, a histogram comprised of the reflectance differences of all pixels located in the cloud-free ice sheet area is calculated (Fig. 4).

In the histogram, the reflectance difference of lake and ice pixels form two distinct populations that can be separated by a properly chosen threshold. For images without lakes, the reflectance differences of ice pixels form an approximately normal distribution (e.g., Fig. 4(a)). For images with lakes, the reflectance differences of lake pixels are higher than that of ice pixels and the histogram exhibits a positive tail (e.g., Fig. 4(b)). To separate the ice and lake pixels, the algorithm prescribes a reflectance difference threshold at a close-to-zero histogram slope (0.01) in the positive (outward) direction along the x-axis of the histogram (i.e., red vertical line in Fig. 4(b)). Pixels whose reflectance difference exceeds the threshold are identified as possible supraglacial lake pixels.

After detecting possible lakes by reflectance difference in each image, the algorithm then verifies real lakes by tracking these possible lakes in sequential images. While reflectance difference detects most lakes, it cannot detect cloud covered lakes and may report false positive lakes due to cloud shadows, wet snow patches, etc. (e.g., 2nd row in Fig. 6). Cloud cover is common in West Greenland during the melt season. For example, (Box & Ski, 2007) studied the region near Jakobshavn Isbrae (67.55°N to 69.96°N, 47.40°W to 51.66°W) from 2000 to 2005 and found on average 4.7 completely cloud-free MOD02 images per month during summer through manual selection. Therefore, partially cloudy images are included in the analysis to fully utilize the regions that are cloud-free (Section 2.2).

However, the cloud masks retrieved from MOD10-L2 are unreliable in identifying small-scale clouds, such as isolated or scattered clouds, over snow and ice covered surfaces (Ault et al., 2006). Thus, a

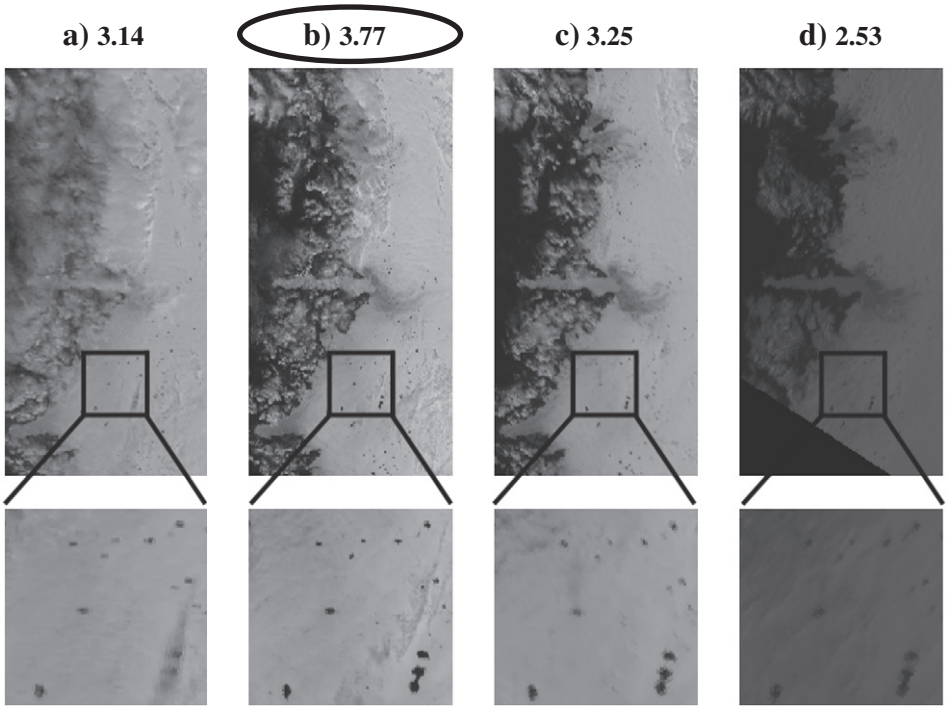

Fig. 3. Illustrative example of quality score: Four images taken on July 4th, 2009 with individual quality scores listed above them. Compared to the cloudy image (a), the less sharp image (c), and the image with low reflectance (d), (b) is the best-quality image with the highest quality score.

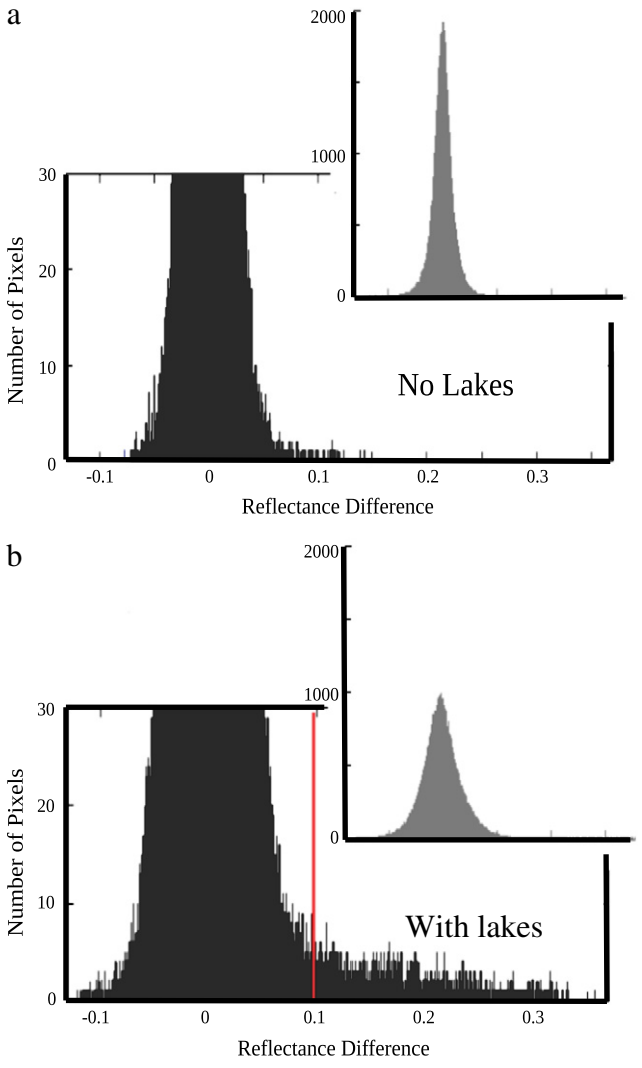

Fig. 4. Histograms of reflectance difference. In both sub-figures, the gray histograms (insets) are overviews and black histograms are zoom-ins. (a) Images without lakes: reflectance difference of ice pixels takes on an approximately normal distribution. (b) Images with lakes: reflectance difference of lake pixels is relatively high and results in a substantial positive tail. Based on the slope of the histogram, the algorithm dynamically determines the reflectance difference threshold (red vertical line in (b)) to best isolate the positive tail (i.e., lakes) from the normal distribution (i.e., ice).

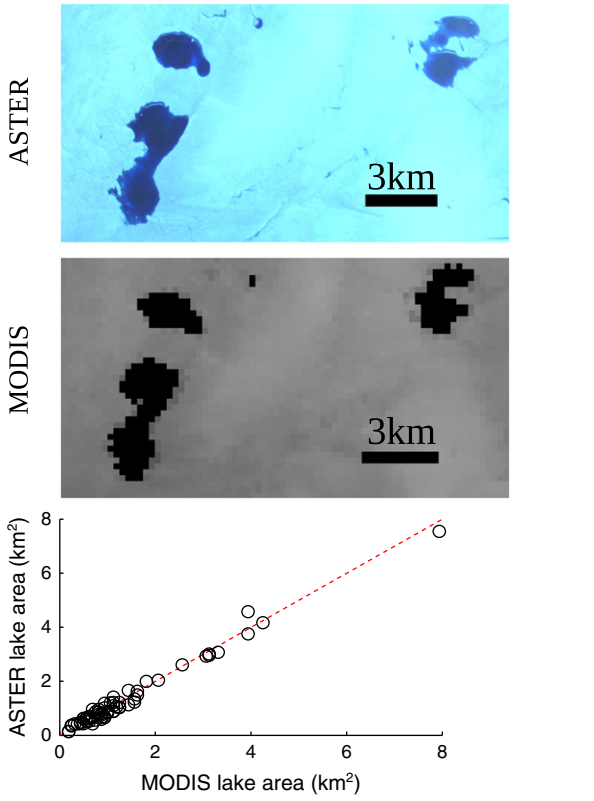

Fig. 5. A subset of supraglacial lakes in corresponding 15 m resolution ASTER (top) and 250 m resolution MODIS (middle) images with classified lake pixels denoted as black. Bottom: relation between lake area in ASTER vs. algorithm-classified lake areas in MODIS (correlation: $r = 0.99$).

supraglacial lake that is located in a cloud-free region in the cloud mask may still be obscured by small-scale clouds not reported by the MOD10-L2 data. This unreliable cloud masking poses a significant challenge when attempting to track individual lakes.

To deal with unexpected and highly transient cloud cover, the algorithm tracks lakes by their temporal consistency in both location and size. Small-scale clouds generally change within minutes or hours while lake area tends to change more slowly, remaining a similar size in the same location for days. For example, if the cloud mask indicates that a given lake location is cloud-free on *Day*1, *Day2* and *Day*3, but the algorithm initially only detects the given lake on *Day*1 and *Day*3, the algorithm concludes that the lake also existed on *Day2*. We then track individual lakes by their temporally-consistent locations and sizes.

Tracking temporally-consistent lakes is performed by pairing "matching lakes" in sequential images. If a given possible lake in two sequential images fully or partially overlaps between images and has a similar area, it is confirmed as one lake. However, if we cannot find its matching lake in the previous and subsequent image, the possible lake is assessed as a noise. Similar lake area is defined as follows; If the algorithm detects a possible lake 1 (area $= A_1$) in one image and another possible lake 2 (area $= A_2$) in the subsequent image, we define A_1 and A_2 as being similar when:

$$0.5A_1 < A_2 \leq 2A_1 + 8 \text{ pixels} \quad (1)$$

The parameters in Eq. (1) were assessed based on the assumption that, for slowly-varying lakes, lake area is expected to neither double nor half in size between consecutive images. The uncertainty of 8 pixels is derived from an uncertainty of 2 pixels in 4 corners.

The concept of temporal consistency (i.e., pairing matching lakes) is also useful for mapping suddenly-changing lakes, such as lakes merging or lakes undergoing full or partial drainage. For most slowly-varying lakes, the algorithm can find their matching lakes with similar area (Eq. (1)) in the subsequent images. For lakes with sudden area changes, their areas are similar to that of lakes in the previous images. For example, assume a possible lake appears from *Day*1 to *Day3* and drains between *Day2* and *Day3*. Because of a dramatic area change, the possible lakes in *Day2* and *Day3* do not satisfy Eq. (1). It does not mean that the possible lake in *Day*2 represents noise, since its area is similar to that of lake in *Day*1. Therefore, unlike transient clouds or noise, a real lake has a matching lake in the following or previous day regardless of sudden changes.

The tracking of an individual lake is performed as follows: (1) A new lake is confirmed if the lake shows up twice within 6 successive days and appears a total of 3 times over the melt season. If, however, the lake has not been seen for 5 days during cloud-free conditions before the 3rd appearance, it is not confirmed as a lake; (2) For an existing lake, if the algorithm can find its matching lake in the previous and subsequent image, the lake is mapped for that particular day; (3) A lake is defined as "disappeared" when the lake has not been seen for 5 days during cloud-free conditions.

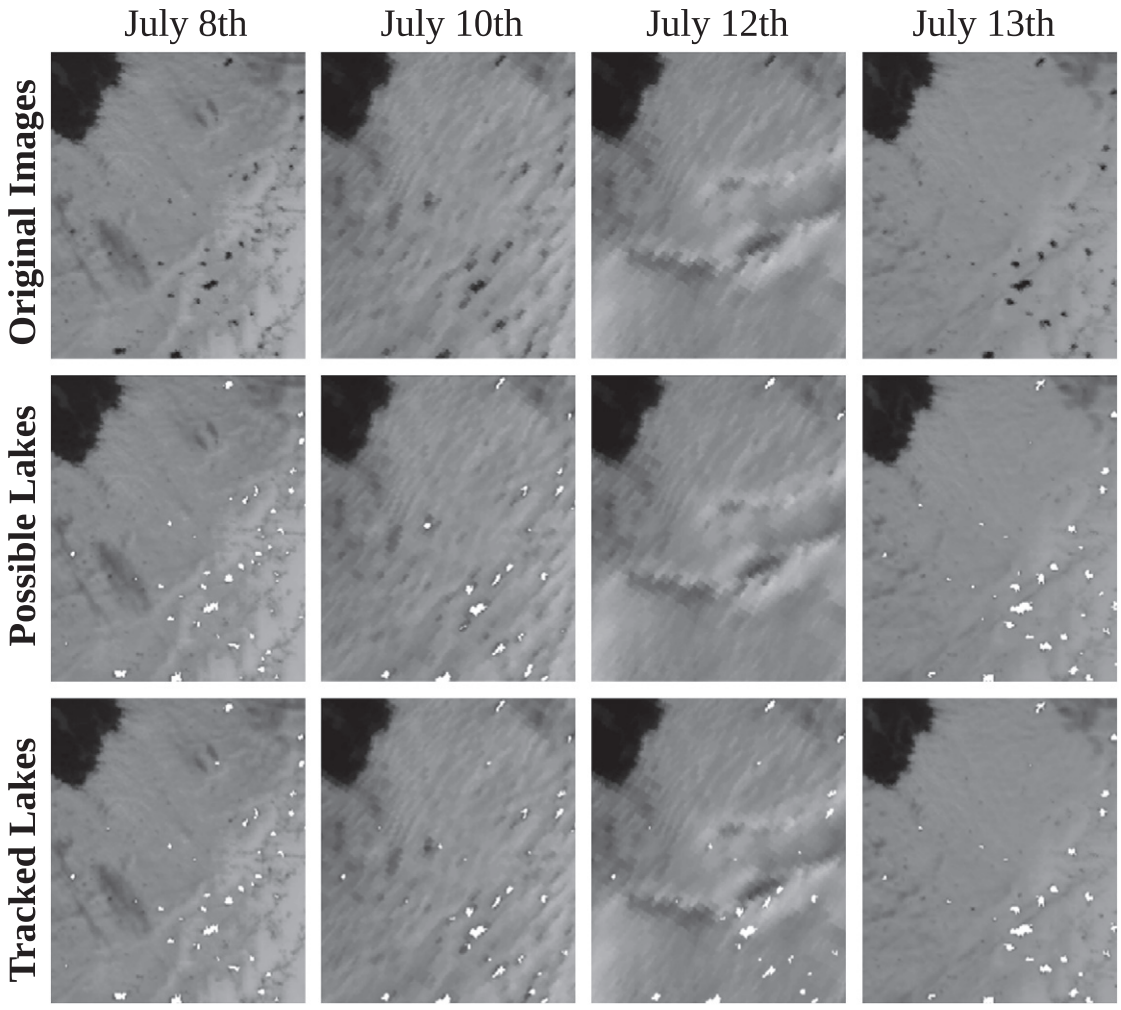

Fig. 6. Illustrative example of tracked lakes: 1st row: Original satellite images (MOD02); 2*nd* row: Images with possible lakes (i.e., whitest pixels) detected by reflectance difference; 3rd row: Images with tracked lakes (i.e., whitest pixels). From left to right column are July 8^{th}, 10^{th}, 12^{th}, and 13^{th} in 2006. In the 2nd row, detecting possible lakes in each image works well in cloud-free images (July 8^{th} and 13^{th}), but not in less sharp (July 10^{th}) and cloudy (July 12^{th}) images. The algorithm robustly tracks lakes in sequential images regardless of this noise (i.e., 3rd row).

These parameters were selected as conservative bounds for the temporal variability of supraglacial lakes. For example, instead of confirming a lake when it appears twice, the algorithm confirms a lake after its third appearance. Confirming a lake disappearance is more difficult due to frequent cloud coverage, as ice and cloud can be indistinguishable in MODIS images. Thus, instead of confirming lake disappearance after a single day of absence, the algorithm confirms a lake disappearance after a five-day absence.

After the initial tracking process, the algorithm removes false positives, such as wet snow patches, shadows of clouds, and other geographic features. This is done by recording the mean reflectance of each individual lake over the observation period. False positives generally have a median reflectance, which is between that of ice/snow (i.e., relatively high reflectance) and lake water (i.e., relatively low reflectance). While some false positives, such as wet snow, do eventually become lakes (i.e., relatively low reflectance), most false positives maintain median reflectance. The range of "relatively low reflectance" is defined as reflectance below the (95^{th} percentile reflectance)/2, where 100^{th} percentile reflectance is the highest value when all reflectances are sorted from low to high in a given image. The algorithm then removes false positive lakes, which have mean reflectances that do not drop to relatively low reflectance value during the melt season. This step automatically removes the false positives that were manually identified by (Selmes et al., 2011).

3. Algorithm performance and output

3.1. Algorithm performance

Fig. 6 is an illustrative example of the algorithm performance. Despite poor image quality due to an oblique satellite viewing angle on July 10^{th} and extensive cloud cover on July 12^{th}, the use of temporal lake mapping between sequential days allows the algorithm to track lakes even when they are obscured by clouds (i.e., 3rd row in Fig. 6). Note, however, instances where lakes that are initially missed in an individual image (i.e., 2nd row) may be successfully tracked in sequential images (i.e., 3rd row).

The accuracy of classified lake area was assessed by comparing lake areas classified in MODIS images (250 m resolution) with that in high resolution ASTER images (15 m resolution, Fig. 5). Because of coarse resolution (250 m), uncertainty in classified lake area in MODIS images could be large. Lake areas in 15 m ASTER images are much more reliable, and may be treated as ground truth. Lake area difference between these two image types therefore represents the error of classified lake area derived from the algorithm. Fig. 5 demonstrates the lake area of 63 classified lakes in these two image types is strongly correlated ($r = 0.99$). The error of classified lake area was quantified by root mean square error (RMSE), which favors smaller lakes (i.e., produces smaller error), and root squared error per 1 km^2

lake (RSE/km^2), which favors bigger lakes. RSE/km^2 is defined as $\sqrt{\sum\left((A_{MODIS}-A_{ASTER})^2\right)}/(\sum A_{MODIS})$, where A_{MODIS} and A_{ASTER} are individual lake areas in MODIS and ASTER images, respectively. For our algorithm, RMSE is 0.20 km^2 and RSE/km^2 is 0.027, which are comparable with classification results reported in previous studies (i.e., 0.22 km^2 and 0.045 in Sundal et al. (2009); 0.11 km^2 and 0.040 in Selmes et al. (2011)).

To assess the lake tracking accuracy in sequential images, we visually validated tracked lakes over a temporal (all images in 2000, 2003, 2006 and 2009, 359 images in total) and spatial subset (36% of the study area) of MODIS imagery. A lake is defined as correctly tracked by the algorithm if visual identification confirms that (1) it is indeed a lake and (2) accurate properties have been reported (such as lake onset and cessation day, lake area, etc.). Results show there is good agreement between the algorithm-tracked and manually-tracked lakes in each year (Table 1). In the evaluation, four types of results were assessed: (*TP*) true positives, which are correctly tracked lakes, both temporally and also by area, (*FN*) false negatives, which are true lakes that the algorithm failed to track, (FP_1) type 1 false positives, which are not true lakes (i.e., bedrock nunataks) that were tracked by the algorithm, and (FP_2) type 2 false positives, which are true lakes that are indeed tracked, but for which incorrect lake properties are reported. False negatives can occur when lakes are very small and appear for only a short period of time.

Tracking accuracy is expressed by recall and precision. Recall = $TP/(TP+FN)$ = (correctly tracked lakes)/(all manually tracked lakes) = 0.990, or 99.0% of supraglacial lakes were successfully found by the tracking algorithm. Precision = $TP/(TP+FP_1+FP_2)$ = (correctly tracked lakes)/(all algorithm-tracked lakes) = 0.963, or 96.3% of reported lakes are supraglacial lakes with accurate lake properties. The algorithm efficiency is characterized by computation time. The algorithm code was implemented in MATLAB R2011a and executed on a workstation with 6 GB memory and an Intel(R) Xeon(R) CPU with 2.27 GHz processor. When provided all 9,040 prepared (i.e., georectified and cropped) MODIS MOD02 images, the algorithm took an average of 477 s (less than 8 min) per melt season to select highest quality images (Section 2.2) and track supraglacial lakes (Section 2.3).

We perform a sensitivity analysis of lake area as a function of threshold value. The primary justification of the threshold technique is that the reflectances of lake and ice pixels are distinct, and form two populations within the reflectance difference histogram (e.g., Fig. 4–(b)). A meaningful threshold, which properly divides these two populations, occurs where the histogram slope approaches zero in the positive (outward) direction along the x-axis of histogram. A threshold slope of 0.01 was used in this study. Imposing a larger threshold slope (i.e., >0.01) would classify more pixels as lake, while imposing a smaller threshold slope (i.e., <0.01) would classify fewer pixels as lake. We assessed the percentage of image area classified as lake pixels in 2009, or "percentage of lake area", over a wide range of threshold slopes (Fig. 7). When the thresholding slope is ≤0.01, the percentage of lake area does not significantly vary (0.19%−0.29%). When the threshold slope approaches 0.1, the percentage of lake area increases significantly (0.82%). The threshold slope we prescribed (0.01) was chosen to minimize the discrepancy between manually delineated and algorithm-derived lake areas. This sensitivity analysis suggests our results: (1) are relatively insensitive to a smaller threshold slope, and (2) an order of magnitude change in threshold slope is required to significantly change our results.

Table 1
Algorithm evaluation.

Year	2000	2003	2006	2009	Average
TP[a]	331	312	282	269	–
FN[a]	6	3	0	3	–
FP_1[a]	4	3	7	5	–
FP_2[a]	4	6	9	7	–
Precision	0.976	0.972	0.946	0.957	0.963
Recall	0.982	0.990	1.000	0.989	0.990

[a] Expressed in "number of lakes".

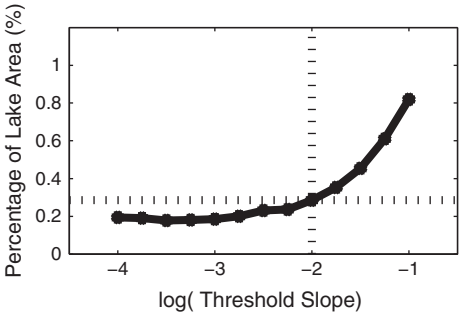

Fig. 7. Average percentage of image area assigned as lake pixels in 2009 (i.e., percentage of lake area) vs. threshold slope. Dash lines denotes the threshold slope used in this study (0.01).

3.2. Interpretation of algorithm output

On an annual basis between 304 and 590 supraglacial lakes were found to form within the ~16,500 km^2 study region in each melt season (mean = 487, standard deviation = 89). For each individual lake, the algorithm recorded (1) lake center coordinates before the lake disappeared, (2) daily lake area, "*A*", (3) date of lake onset, "j_o", (4) date of lake cessation, "j_c", (5) which days are cloudy at the lake location between j_o and j_c, (6) daily mean MODIS band 1 (620 nm to 670 nm) reflectance, as well as (7) lake merge/split events. It is important to note that, due to the relatively coarse spatial resolution of the MODIS imagery (250 m), the algorithm only tracks lakes with an area larger than 2 pixels (i.e., >0.125 km^2).

As we are using visual band imagery, lakes that are covered by ice which is sufficiently thick to have the same optical properties as the surrounding ice, cannot be detected. This limitation is implicit in all previous studies that used optical imagery (Box & Ski, 2007; Lampkin & VanderBerg, 2011; McMillan et al., 2007; Selmes et al., 2011; Sundal et al., 2009).

A set of supraglacial lake parameters were then derived from the algorithm output. Lake center coordinates, on the date of lake cessation, were used to determine lake elevation (z) from a photoclinometry-enhanced digital elevation model (DEM) of Greenland ice sheet with a nominal horizontal resolution of 625 m (Scambos & Haran, 2002). Maximum lake area (A_{max}) was defined as the maximum lake area obtained by a given lake during the melt season. Lake duration (D) was determined by differencing the dates of lake onset and cessation for each lake (i.e., $D = j_c - j_o$). The high temporal resolution of the MODIS dataset allows the rate of change in lake area ($\tilde{A}$; in km^2/d where d is "day") to be determined for each individual lake between consecutive images. This was accomplished by dividing the difference in observed area of a given lake between two successive MODIS images by the time period between the images (i.e., $\tilde{A} = \triangle A/\triangle t$).

The uncertainty of each supraglacial lake parameter was conservatively estimated. While the nominal temporal resolution of detected lakes is one day, the actual period between sequential images can exceed one day due to missing data or cloudy imagery. Therefore, the mean interval between any two consecutive and available MODIS images in each melt season is taken to represent the uncertainty in the dates of lake onset and cessation (δj), ranging between 1 and 3 days depending on the year. Following standard error propagation analysis for operations involving addition or subtraction, uncertainty in annual lake duration (δD) is taken as twice this value (i.e., $\delta D = 2\delta j$). The stated root-mean-squared error of the DEM (±10 m)

is taken to represent the uncertainty in lake elevation (δz). In order to assess lake area uncertainty (δA), we assume an approximately circular lake geometry (Georgiou et al., 2009; Sundal et al., 2009) and apply an uncertainty of a half-pixel width (125 m) to the circumference of each lake. Uncertainty in the rate of change of lake area ($\delta\tilde{A}$) is taken as uncertainty in lake area divided by uncertainty in date (i.e., $\delta\tilde{A} = \delta A/\delta j$).

The annual distributions of supraglacial lake parameters were examined in the context of annual melt intensity (I), defined as annual positive degree days (PDDs) following (Georgiou et al., 2009). Annual PDD values are defined as the time integral of air temperatures above 0 °C in a given year and have units of °C·d (Hock, 2005). For example, ten days with a mean air temperature of 1 °C and one day with a mean air temperature of 10 °C are both equivalent to 10 PDDs. Thus, years with warmer temperatures represent more intense melt years. Hourly air temperatures recorded at Swiss Camp (1152 masl, 69.56°N, 49.34°W, Fig. 1) were used to calculate annual PDDs from 2000 to 2009. According to Spearman's rank correlation coefficient for non-normal populations (ρ), the air temperatures observed at Swiss Camp between 2000 and 2010 are highly correlated to the air temperatures observed at three other weather stations that are located over a broad elevation range within and near the study region: JAR2 (500 mASL; $\rho = 0.92$; ~33 km SW, or southwest of Swiss Camp), JAR1 (913 mASL; $\rho = 0.93$; ~16 km SW), and Crawford Point (1950 mASL; $\rho = 0.89$; ~96 km NE) (Steffen & Box, 2001; Fig. 1; Fig. 8). Thus, the air temperature observed at Swiss Camp may be considered representative of the study region (Fig. 1).

We limit the scope of the following results to supraglacial lakes that are >1 km^2 and reside at elevations above 750 m. The reasons are (1) moulins are less likely to form from smaller lakes, which are less likely to have sufficient water volume (c.f. Van der Veen (2007)), and (2) lakes at lower elevation can be expected to exhibit reduced inter-annual variability in response to inter-annual variations in melt intensity. To normalize the comparison of lake parameters between years with different numbers of lakes, we aggregate each year of lake elevation, maximum area and rate of change of lake area data into normalized nonparametric distributions (i.e., probability density or cumulative density functions). This allows the inter-annual variability of different percentiles of lake elevation (z), maximum lake area (A_{max}) and rate of change of lake area ($\tilde{A}$) to be examined in the context of annual melt intensity. Each year's individual dates of lake onset and cessation, as well as lake duration, are expressed as mean annual values ($\bar{j}_o$, $\bar{j}_c$, and $\bar{D}$ respectively).

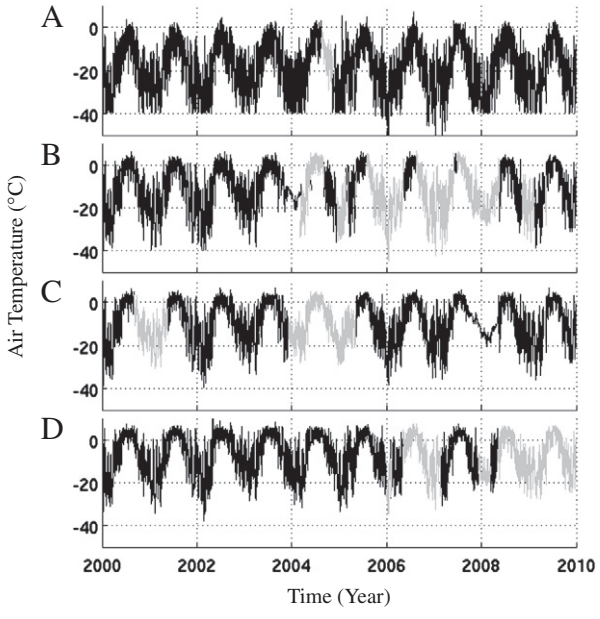

Fig. 8. Observed (black lines) and statistically interpolated (gray lines) air temperature at Crawford Point (A; 1950 mASL), Swiss Camp (B; 1106 mASL), JAR1 (C; 913 mASL) and JAR2 (D; 500 mASL) between 2000 and 2010.

4. Results: supraglacial lake variability

Figs. 9 to 12 summarize the annual distributions of several supraglacial lake parameters versus annual melt intensity. In these figures, line colors are proportional to melt intensity: red denoting the "warmest" year with the most intense melt and blue denoting the "coolest" year with the least intense melt. When examining potential correlations between annual melt intensity and various lake parameters over the ten-year study period, we assess the correlation coefficient (r) with nine degrees of freedom ($df = 9$) and seek a significance level of $p < 0.05$. The p (i.e., p-value) is the probability of getting a correlation as large as the observed value by random chance: $p = 1.0$ indicates a random distribution with no correlation while $p = 0.0$ indicates a true correlation. Significant correlations are denoted as solid lines and the insignificant ones are shown as dashed lines. All the values of correlation coefficients (r), p-values (p), and slopes of regression lines are summarized in Table 2.

Various percentiles of maximum lake area (A_{max}) for each observational year were correlated with annual melt intensity (Fig. 9). We find no significant correlation between annual melt intensity and the 25th, 50th and 75th percentiles of maximum lake area during the 2000 to 2009 period (Table 2). We interpret this as suggesting

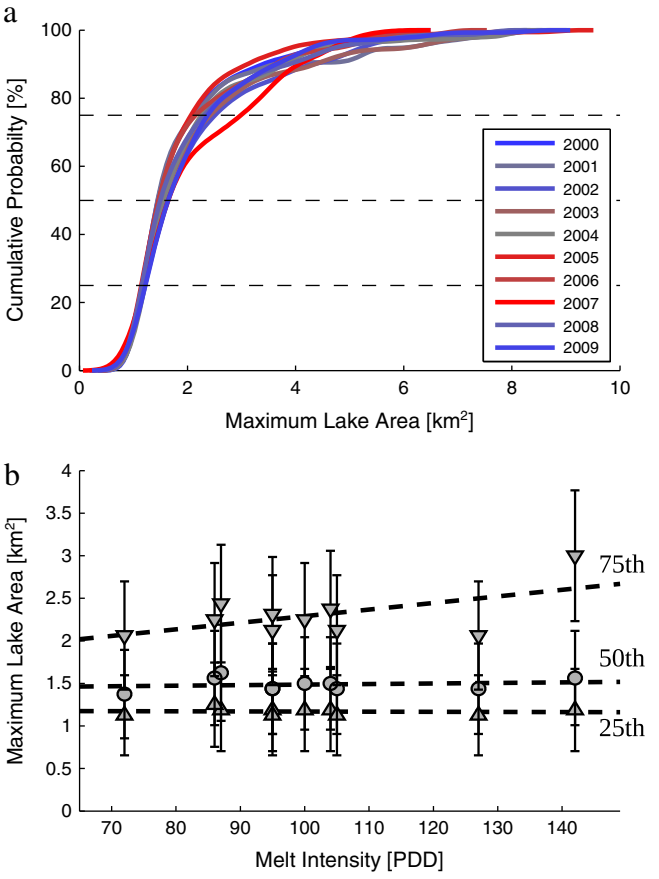

Fig. 9. (a) Cumulative percentile histogram of maximum lake area (A_{max}) for each observational year (line color is proportional to melt intensity, red is the warmest year and blue is the coolest year). (b) Values of the 25th, 50th, and 75th percentiles of annual maximum lake area (△, o, and ▽ respectively) versus annual melt intensity. All three relations are not significant. Vertical error bars denote uncertainty in lake area (δA).

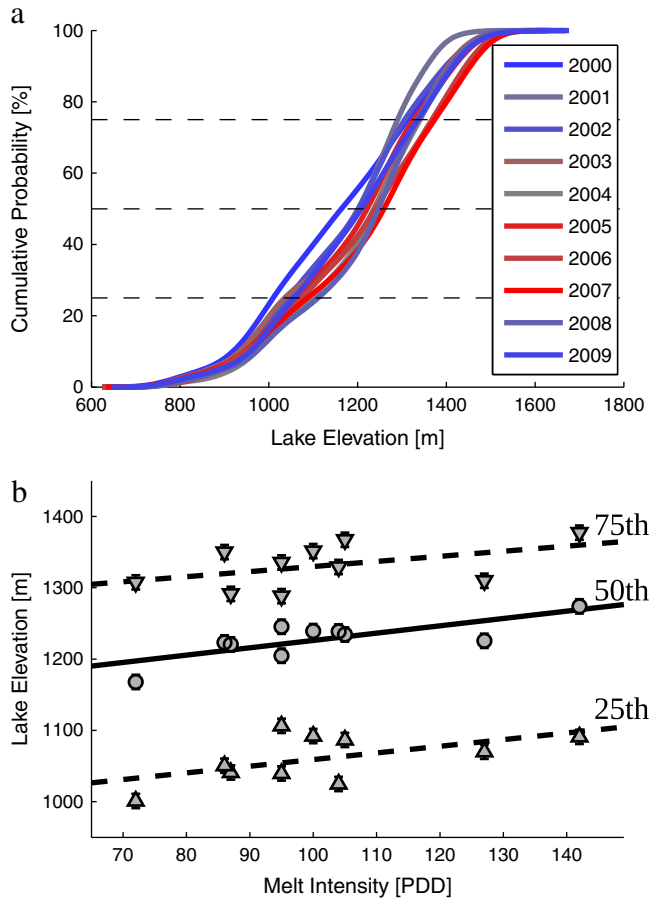

Fig. 10. (a) Cumulative percentile histogram of lake elevation (z) for each observational year (line color proportional to melt intensity, red is the warmest year and blue is the coolest year). (b) Annual values of the 25^{th}, 50^{th}, and 75^{th} percentiles of lake elevation (△, o, and ▽ respectively) versus annual melt intensity. Only the 50^{th} percentile demonstrates a significant relation with melt intensity ($r=0.75$). Insignificant relations are denoted with dashed lines. Vertical error bars denote uncertainty in lake elevation (δz).

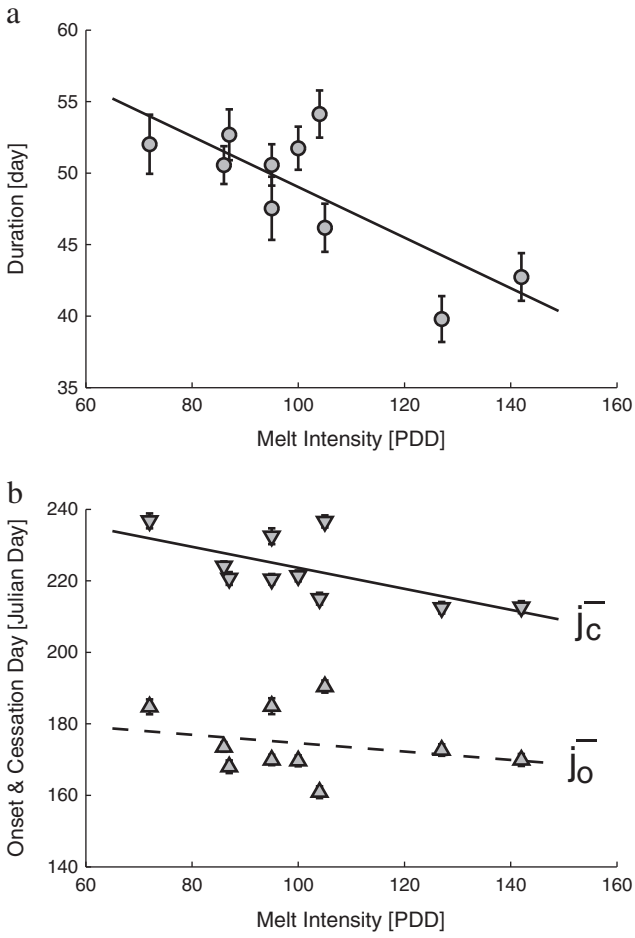

Fig. 11. (a) Mean lake duration ($\bar{D}$) versus annual melt intensity. A significant relation ($r=-0.77$) is denoted with the solid line. Vertical error bars denote uncertainty in mean lake duration (δD). (b) Mean lake onset ($\bar{j}_o$, △) and cessation dates ($\bar{j}_c$, ▽) versus annual melt intensity. Insignificant ($\bar{j}_o$) and significant ($\bar{j}_c$, $r=-0.65$) relations are denoted with dashed and solid lines respectively. Vertical error bars denote uncertainty in date (δj).

that maximum supraglacial lake area neither increases nor decreases as a function of annual melt intensity in the Jakobshavn Isbrae region above 750 m in elevation.

Fig. 10 shows the relation between various percentiles of lake elevation (z) and annual melt intensity for each observational year. The 50^{th} percentile of lake elevation (i.e., solid line in Fig. 10(b)) shows a significant correlation with annual melt intensity ($r=0.75$, Table 2). The 25^{th} and 75^{th} percentiles, however, do not exhibit significant correlations with melt intensity (Table 2). The difference in behavior between the 50^{th} and $25^{th}/75^{th}$ percentiles of lake elevation is discussed in Section 5.

The relation between mean lake duration ($\bar{D}$) and annual melt intensity is shown in Fig. 11(a). Between 2000 and 2009, mean lake duration exhibited a significant negative correlation with melt intensity ($r=-0.77$, Table 2). In contrast to previous findings (Sundal et al., 2009), this counter-intuitively suggests that increasing annual melt intensity results in a shorter melt season duration for supraglacial lakes. Supraglacial lakes become inactive by the winter through one of three mechanisms: (1) freezing over, (2) draining via supraglacial channels to neighboring lakes, and (3) draining via moulins to the subglacial system. Increasing melt intensity is expected to delay freezing over and lengthen the active duration of lakes. Thus, the observation of a shorter active duration under increased melt intensity must reflect a sufficiently large population shift towards earlier supra- or subglacial lake drainage, that outpaces the delay in freeze-over. This notion is supported by Fig. 11(b), which shows the relation between mean onset ($\bar{j}_o$) and cessation ($\bar{j}_c$) dates and annual melt intensity. The mean onset date does not exhibit a significant correlation with annual melt intensity ($\bar{j}_o$ in Table 2) while the mean cessation date does ($\bar{j}_c$: $r=-0.65$, Table 2).

The annual distributions of the rate of change of lake area ($\tilde{A}$) allows the relation between annual melt intensity and $\tilde{A}$ to be assessed (Fig. 12). For illustrative purposes, we correlate annual melt intensity with two extreme events of equal magnitude but opposite sign: rapid lake draining ($\tilde{A}_e^-$: $\tilde{A}\leq -1.3$ km^2/d) and filling ($\tilde{A}_e^+$: $\tilde{A}\geq +1.3$ km^2/d) in Fig. 12. Between 2000 and 2009, the probability of rapid lake drainage events, "$p(\tilde{A}_e^-)$", is always greater than that of rapid lake filling events, "$p(\tilde{A}_e^+)$" (Fig. 12(b)). In addition, the probabilities associated with both extreme events demonstrate significant correlations with annual melt intensity (i.e., $p(\tilde{A}_e^-)$: $r=0.80$; $p(\tilde{A}_e^+)$: $r=0.86$; Table 2). During more intense melt years, supraglacial lakes experience both large draining and filling events more frequently. The slopes of these regressions are approximately equal ($\triangle p(\tilde{A}_e^+)/\triangle I=0.00023/PDD$; $\triangle p(\tilde{A}_e^-)/\triangle I=0.00026/PDD$, Table 2). These regression slopes suggest that an increase in annual melt intensity of 100 PDD increases the probability of extreme drainage event ($\tilde{A}\leq -1.3$ km^2/d) by ~2.6%.

In addition, Fig. 13 demonstrates the recurrence frequency of all lakes that appeared between 2000 and 2009 in the study area (whereby recurrence frequency is defined as the number of years

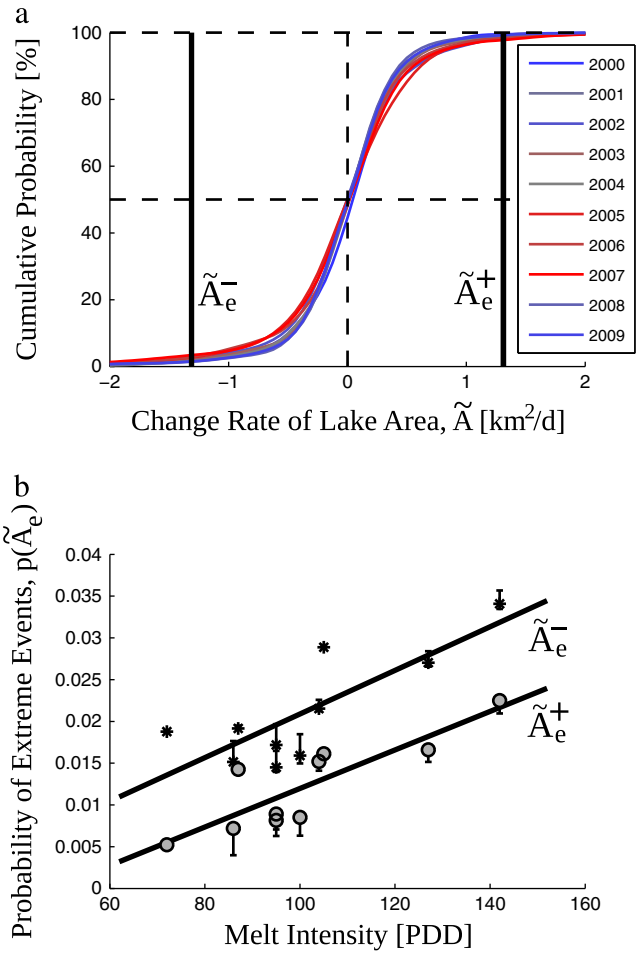

Fig. 12. (a) Cumulative percentile histogram of rate of change of lake area ($\tilde{A}$) for each observational year (line color proportional melt intensity, red is the warmest year and blue is the coolest year). Vertical lines denotes two extreme events: $\tilde{A}_e^-$ (rapid lake draining: $\tilde{A} \leq -1.3$ km^2/d) and $\tilde{A}_e^+$ (rapid lake filling: $\tilde{A} \geq +1.3$ km^2/d). (b) Probability associated with $\tilde{A}_e^-$ (*) and $\tilde{A}_e^+$ (o) events versus annual melt intensity. Both are significant relations ($p(\tilde{A}_e^-)$: $r = 0.80$; $p(\tilde{A}_e^+)$: $r = 0.86$). Vertical error bars denote the uncertainty associated with the probability in the rate of change of lake area ($\pm\delta\tilde{A}$).

Table 2
Relations of lake parameters vs. annual melt intensity (air temperature).

Fig. 9	Maximum lake area (A_{max})		
	25^{th}%	50^{th}%	75^{th}%
r	−0.07	0.17	0.57
p	0.84	0.64	0.09
Fig. 10	**Lake Elevation (z)**		
	25^{th}%	50^{th}%	75^{th}%
r	0.55	* **0.75**	0.47
p	0.10	* **0.01**	0.17
s	–	1.03 (m/PDD)	–
Fig. 11	**Duration ($\bar{D}$)**	**Onset date ($\bar{j}_o$)**	**Cessation date ($\bar{j}_c$)**
r	* **−0.77**	−0.26	* **−0.65**
p	* **0.009**	0.47	* **0.04**
s	−0.18 (d/PDD)	–	−0.29 (d/PDD)
Fig. 12	**Rapid drainage, $p(\tilde{A}_e^-)$**		**Rapid filling, $p(\tilde{A}_e^+)$**
r	* **0.80**		* **0.86**
p	* **0.005**		* **0.001**
s	0.00026 (1/PDD)		0.00023 (1/PDD)

* (bold font): Significant relation ($p<0.05$).
r: Correlation coefficient, p: p-value.
s: Regression Slope = △ (lake parameter) / △ (melt intensity).

that a given lake is active divided by ten years). The statistics show that larger lakes appear more frequently than smaller lakes. For example, the average area of lakes with a recurrence frequency of ~1 (i.e., appear every year) is 2 km^2, while the average area of lakes with a recurrence frequency of ~0.1 (i.e., appear only once in 10 years) is 0.5 km^2 (Fig. 13(b)). Only a small portion of lakes (13.2%) reappear every year within the study region. (Fig. 13(a)).

5. Discussion

The positive correlation between annual median lake elevation and annual melt intensity indicates that lakes are more active at higher elevations during warmer or more intense melt years (Fig. 10). This suggests that higher elevation regions which normally do not experience rapid surface-to-bed hydrologic connectivity, become more susceptible to moulin creation via supraglacial lake drainage events during more intense melt years (Shepherd et al., 2009; Sundal et al., 2009). We speculate, however, that the absence of a positive correlation between annual 25^{th} percentile lake elevation and melt intensity is due to the abundance of perennial lakes in the lower elevation portion of the study area. The perennial lakes, which form in both low and high melt intensity years, are expected to result in low sensitivity to annual variations in melt intensity at these lower elevations. We interpret this as suggesting that only supraglacial lakes above ~1050 m (i.e., the approximate 25^{th} elevation percentile) exhibit strong inter-annual variability in response to variations in annual melt intensity. Additionally, we speculate that the absence of a significant correlation between annual 75^{th} percentile of lake elevation and melt intensity is due to the presence of an upper elevation limit imposed on the lake distribution; this upper elevation limit could be physical or artificial. A physical upper elevation limit may stem from the upstream boundary of basal sliding. Bedrock depressions are believed to be responsible for the ice surface depressions that form supraglacial lake catchments (Echelmeyer et al., 1991; Thomsen et al., 1988). As bedrock topography is only expressed in ice surface topography in regions experiencing basal sliding (Gudmundsson, 2003), interior regions of the ice sheet that do not experience basal sliding are unlikely to contain ice surface depressions suitable for lake formation. An artificial upper elevation limit might stem from the study area failing to reach sufficiently far inland/upglacier (i.e., >1700 m elevation; (Sundal et al., 2009)) to capture the behavior of the uppermost quartile of lake elevation.

Supraglacial lakes have been observed to increase in size throughout one or several melt seasons until a critical water pressure is achieved, at which time they drain rapidly, presumably through hydrofracture (Box & Ski, 2007; Das et al., 2008; Georgiou et al., 2009; Van der Veen, 2007). If the water pressure (or lake depth) required to initiate hydrofracture and rapid drainage is viewed as a threshold value, it should not be expected to vary with annual melt intensity (Krawczynski et al., 2009). As lake area is a reasonable proxy for lake volume (described in the following paragraph), the absence of a significant correlation between lake area and annual melt intensity (Fig. 9) may be interpreted as evidence of no significant change in lake volume in response to variations in annual melt intensity. Thus, we believe that supraglacial lakes in West Greenland are compensating for observed increases in surface meltwater production over the study decade (Hanna et al., 2005; Tedesco, 2007) by increasing the frequency of lake drainage events rather than increasing supraglacial water storage. The observation of earlier mean lake cessation dates with increasing melt intensity supports this notion (Fig. 11). The observation that lakes experience extreme drainage events (i.e., $\tilde{A} \leq -1.3$ km^2/d) more frequently during more

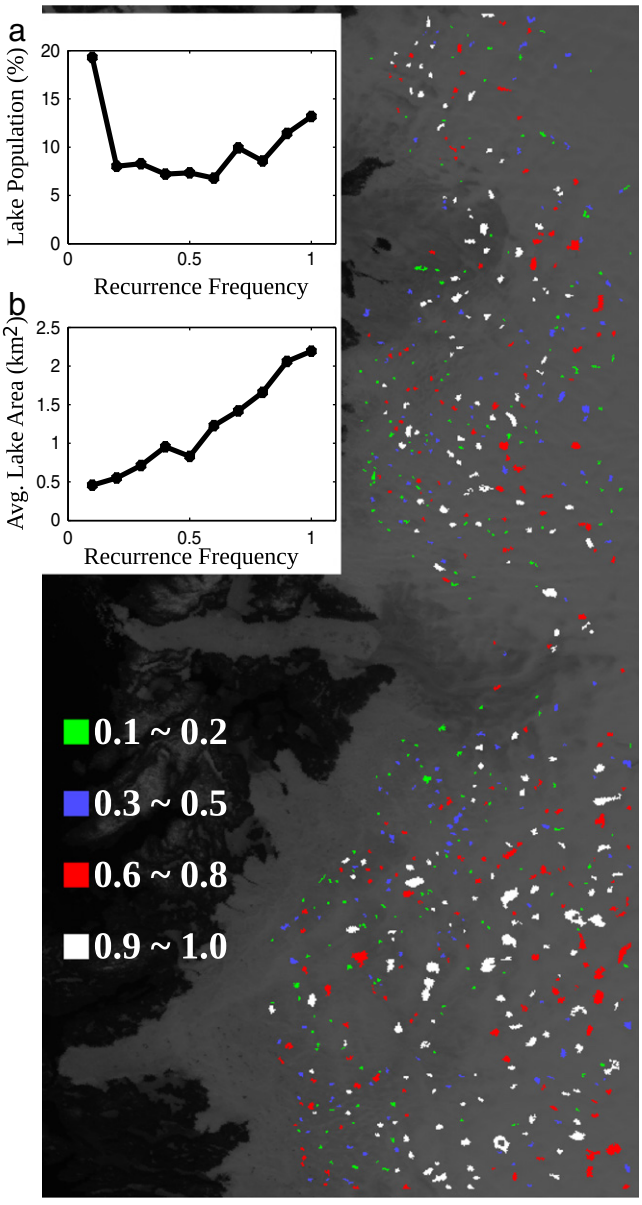

Fig. 13. Recurrence frequency of all lakes that appeared between 2000 and 2009 in the study area, whereby recurrence frequency is number of years that a given lake is active divided by study period (i.e., 10 years). Inset (a): Percentage of lake population (i.e., number of lakes of a certain recurrence frequency divided by the number of all lakes) vs. recurrence frequency. Inset (b): Average lake area vs. recurrence frequency.

intense melt years also supports the inference that the "slow-fill rapid-drain" lifecycle (Box & Ski, 2007; Georgiou et al., 2009; Krawczynski et al., 2009) has accelerated to accommodate increased surface meltwater production (Fig. 12). The positive correlation between extreme lake filling events (i.e., $\tilde{A} \geq +1.3$ km^2/d) and annual melt intensity likely reflects an earlier transition from relatively slow snow melt runoff to relatively quick ice melt runoff in more intense melt years (Georgiou et al., 2009; Sundal et al., 2009). An earlier snow-to-ice runoff transition would also be expected to aid lakes in achieving critical water pressures earlier in the melt season during more intense melt years.

Lake area is a reasonable proxy for lake volume. Several studies have used the fact that visible band radiation becomes increasingly attenuated with water depth to quantify lake volume from space borne data (Box & Ski, 2007; Georgiou et al., 2009; Sneed & Hamilton, 2007; Tedesco & Steiner, 2011). We suggest that there is also a theoretical basis to expect lake volume to be highly dependent on lake area. If supraglacial lake geometry is simplified to an upside cone (e.g., Krawczynski et al. (2009)) with a diameter to depth ratio α, lake volume (V) could be expressed as: $V = \pi\alpha D^3/12$, where D is lake diameter. Similarly, lake area (A) may be expressed as: $A = \pi D^2/4$. Substituting D yields: $V = (2\alpha/3\sqrt{\pi})A^{3/2}$. This suggests that lake volume is linearly dependent on diameter to depth ratio (α) and non-linearly dependent on lake area (A). While A can vary over orders of magnitude (Box & Ski, 2007), α likely varies over a relatively small range constrained by variations in ice surface topography (lakes tend to form in shallow surface depressions that reflect the transmission of long wavelength bedrock topography features to the ice surface; (Echelmeyer et al., 1991)). Thus, lake volume can be expected to be more dependent on lake area than diameter to depth ratio. Previously published lake area observations and volume estimates confirm that lake volume is significantly correlated with lake area (i.e., $p<0.01$, $r=0.79$ and $df=29$ from Tables 5 and 6 in Box & Ski (2007)). We therefore take lake area as a proxy for lake volume, and interpret the absence of a significant correlation between lake area and annual melt intensity (Fig. 9) as evidence of no significant change in supraglacial lake volume in response to variations in annual melt intensity.

6. Conclusion

In this study we observed a large population of supraglacial lakes in West Greenland over ten consecutive melt seasons (2000 to 2009). We developed a robust algorithm to automatically track supraglacial lakes using visible MODIS imagery through time. The algorithm operates in a four-step process: (1) selecting the highest quality MODIS image within each day, (2) applying an adaptive threshold to detect individual lakes in images of diverse quality, (3) tracking identified lakes individually, as lakes appear/disappear, increase/decrease in area and merge/split, and (4) removing false positives automatically. The algorithm achieves high accuracy in tracking supraglacial lakes through time: 99.0% of supraglacial lakes can be detected and tracked by our algorithm and 96.3% of reported lakes are supraglacial lakes with accurate lake properties.

The parameters of lake onset and cessation, lake elevation, maximum lake area and rate of change of lake area, were examined in the context of in situ annual melt intensity observations, where a higher annual melt intensity represents a year with warmer temperatures (and hence more intense meltwater production). Our findings suggest that, in warmer years, lakes experience more extreme drainage and filling events and a shorter mean lake duration (as lakes disappear earlier). Annual maximum lake area, which we take as a proxy for annual maximum lake volume, exhibits no significant correlation with annual melt intensity between 2000 and 2009. We interpret this as suggesting that supraglacial lakes accommodate increased surface meltwater production during warmer years by draining more frequently and earlier in the melt season. Additionally, the lake population extends to higher elevations during warmer years. In other words, extreme lake drainage events (and corresponding surface-to-bed hydrologic connections via moulins) can be expected to occur more frequently over a larger area of Greenland Ice Sheet in a warmer climate. It is unclear whether the expected increase in the spatial and temporal frequency of surface-to-bed hydrologic connections will increase (e.g. (Zwally et al., 2002)) or decrease (e.g. (Sundal et al., 2011)) the regional annual ice displacement due to basal sliding (via a net increase in basal lubrication or an earlier seasonal transition to efficient subglacial drainage, respectively).

Acknowledgments

This work was supported by the National Science Foundation (NSF) grant ARC 0941442 to J.S., D.G. and Q.L. We thank the National Aeronautics and Space Administration (NASA) for freely providing

MODIS data from the Warehouse Inventory Search Tool (WIST). Y.L. thanks David Fanning for his advice and assistance during the early stages of this project. W.C. thanks the Natural Science and Engineering Research Council (NSERC) of Canada and the Cooperative Institute for Research in Environmental Sciences (CIRES) for fellowship support. We thank Doug MacAyeal for an insightful collegial review of an earlier version of this manuscript.

References

Ault, T., Czajkowski, K., Benko, T., Coss, J., Struble, J., Spongberg, A., et al. (2006). Validation of the MODIS snow product and cloud mask using student and NWS cooperative station observations in the Lower Great Lakes Region. *Remote Sensing of Environment*, 341–353.

Bartholomew, I., Nienow, P., Mair, D., Hubbard, A., King, M., & Sole, A. (2010). Seasonal evolution of subglacial drainage and acceleration in a Greenland outlet glacier. *Nature Geoscience*, 408–411.

Box, J., & Ski, K. (2007). Remote sounding of Greenland supraglacial melt lakes: Implications for subglacial hydraulics. *Journal of Glaciology*, 257–265.

Cazenave, A., & Llovel, W. (2010). Contemporary sea level rise. *Annual Review of Marine Science*, 145–173.

Colgan, W., Steffen, K., McLamb, W., Abdalati, W., Rajaram, H., Motyka, R., et al. (2011). An increase in crevasse extent, West Greenland: Hydrologic implications. *Geophysical Research Letters*, L1850.

Das, S., Joughin, I., Behn, M., Howat, I., King, M., Lizarralde, D., et al. (2008). Fracture propagation to the base of the Greenland ice sheet during supraglacial lake drainage. *Science*, *320*, 778.

Echelmeyer, K., Clarke, T., & Harrison, W. (1991). Surficial glaciology of Jakobshavns Isbræ, West Greenland: Part I. Surface morphology. *Journal of Glaciology*, 368–382.

Georgiou, S., Shepherd, A., McMillan, M., & Nienow, P. (2009). Seasonal evolution of supraglacial lake volume from ASTER imagery. *Annals of Glaciology*, 95–100.

Gudmundsson, G. (2003). Transmission of basal variability to a glacier surface. *Journal of Geophysical Research*, 2253.

Hall, D., Riggs, G., & Salomonson, V. (2006). *MODIS/Terra snow cover 5-min L2 swath 500 m V005.* updated daily. Boulder, Colorado USA: National Snow and Ice Data Center, Digital media [May to October, 2000 to 2010].

Hall, D., Riggs, G., & Salomonson, V. (2007). *MODIS/Aqua Snow Cover 5-min L2 Swath 500 m V005.* updated daily. Boulder, Colorado USA: National Snow and Ice Data Center, Digital media [May to October, 2000 to 2010].

Hanna, E., Huybrechts, P., Janssens, I., Cappelen, J., Steffen, K., & Stephens, A. (2005). Runoff and mass balance of the Greenland ice sheet: 1958–2003. *Journal of Geophysical Research*, D13108.

Haran, T. (2003). *MS2GT: The MODIS Swath-to-Grid Toolbox.* .

Hock, R. (2005). Glacier melt: A review of processes and their modelling. *Progress in Physical Geography*, 362–391.

Hoffman, M. J., Catania, G. A., Neumann, T. A., Andrews, L. C., & Rumrill, J. A. (2011). Links between acceleration, melting, and supraglacial lake drainage of the western Greenland Ice Sheet. *Journal of Geophysical Research*, *116*, F04035.

Joughin, I., Das, S., King, M., Smith, B., Howat, I., & Moon, T. (2008). Seasonal speedup along the western flank of the Greenland Ice Sheet. *Science*, *320*, 781–783.

Joughin, I., Tulaczyk, S., Fahnestock, M., & Kwok, R. (1996). A mini-surge on the Ryder Glacier, Greenland, observed by satellite radar interferometry. *Science*, *274*, 228–230.

Krawczynski, M., Behn, M., Das, S., & Joughin, I. (2009). Constraints on the lake volume required for hydro-fracture through ice sheets. *Geophysical Research Letters*, 1–5.

Lampkin, D., & VanderBerg, J. (2011). A preliminary investigation of the influence of basal and surface topography on supraglacial lake distribution near Jakobshavn Isbrae, western Greenland. *Hydrological Processes*, doi:10.1002/hyp. 8170.

McMillan, M., Nienow, P., Shepherd, A., Benham, T., & Sole, A. (2007). Seasonal evolution of supra-glacial lakes on the Greenland Ice Sheet. *Earth and Planetary Science Letters*, 484–492.

Pimentel, S., & Flowers, G. (2011). A numerical study of hydrologically driven glacier dynamics and subglacial flooding. *Proceedings of the Royal Society A: Mathematical, Physical and Engineering Science*, 537–558.

Scambos, T., & Haran, T. (2002). An image-enhanced DEM of the Greenland Ice Sheet. *Annals of Glaciology*, 291–298.

Schoof, C. (2010). Ice-sheet acceleration driven by melt supply variability. *Nature*, *468*, 803–806.

Selmes, N., Murray, T., & James, T. (2011). Fast draining lakes on the Greenland Ice Sheet. *Geophysical Research Letters*, L15501.

Shepherd, A., Hubbard, A., Nienow, P., King, M., McMillan, M., & Joughin, I. (2009). Greenland ice sheet motion coupled with daily melting in late summer. *Geophysical Research Letters*, L01501.

Shepherd, A., & Wingham, D. (2007). Recent sea-level contributions of the Antarctic and Greenland ice sheets. *Science*, *315*, 1529–1532.

Sneed, W., & Hamilton, G. (2007). Evolution of melt pond volume on the surface of the Greenland Ice Sheet. *Geophysical Research Letters*, L03501.

Steffen, K., & Box, J. (2001). Surface climatology of the Greenland ice sheet—Greenland Climate Network 1995–1999. *Journal of Geophysical Research. D. Atmospheres*, *106*, 33,951–33,964.

Sundal, A., Shepherd, A., Nienow, P., Hanna, E., Palmer, S., & Huybrechts, P. (2009). Evolution of supra-glacial lakes across the Greenland Ice Sheet. *Remote Sensing of Environment*, 2164–2171.

Sundal, A., Shepherd, A., Nienow, P., Hanna, E., Palmer, S., & Huybrechts, P. (2011). Melt-induced speed-up of Greenland ice sheet offset by efficient subglacial drainage. *Nature*, *469*, 521–524.

Tedesco, M. (2007). Snowmelt detection over the Greenland ice sheet from SSM/I brightness temperature daily variations. *Geophysical Research Letters*, L02504.

Tedesco, M., & Steiner, N. (2011). In-situ multispectral and bathymetric measurements over a supraglacial lake in western Greenland using a remotely controlled watercraft. *The Cryosphere*, 445–452.

Thomsen, H., Thorning, L., & Braithwaite, R. (1988). Glacier-hydrological conditions on the Inland Ice north–east of Jakobshavn/Illulissat, West Greenland. *Grønlands Geologiske Undersøgelse Rapport, 138*.

Van de Wal, R., Boot, W., Van den Broeke, M., Smeets, C., Reijmer, C., Donker, J., et al. (2008). Large and rapid melt-induced velocity changes in the ablation zone of the Greenland Ice Sheet. *Science*, *321*, 111–113.

Van den Broeke, M., Bamber, J., Ettema, J., Rignot, E., Schrama, E., Van de Berg, W., et al. (2009). Partitioning recent Greenland mass loss. *Science*, *326*, 984–986.

Van der Veen, C. (2007). Fracture propagation as means of rapidly transferring surface meltwater to the base of glaciers. *Geophysical Research Letters*, L01501.

Warren, S. (1982). Optical properties of snow. *Technical Report DTIC Document*.

Zwally, H., Abdalati, W., Herring, T., Larson, K., Saba, J., & Steffen, K. (2002). Surface melt-induced acceleration of Greenland ice-sheet flow. *Science*, *297*, 218–222.